photonics

MDPI

Review

Monolayer Optical Metasurface Design from Single-Function to Multi-Functions

Ailing Li [1,*], Zhe Bai [2], Zhe Xu [2] and Xin Wang [1]

[1] Yantai Vocational College, Yantai 264670, China; 20220006@ytvc.edu.cn
[2] Xi'an Institute of Optics and Precision Mechanics, Chinese Academy of Sciences, Xi'an 710119, China; baizhe@opt.ac.cn (Z.B.); xuzhe@opt.ac.cn (Z.X.)
* Correspondence: a20210059@ytvc.edu.cn

Abstract

Over the past decade, metasurfaces have offered significant promise for miniaturized and flat photonics by enabling precise manipulation of light's phase, amplitude, and polarization through geometric design. The pursuit of multifunctional wavefront modulation at the micro-nano scale using these surfaces has emerged as a prominent research area. In this paper, we first explore the phase modulation principles underlying meta-atoms, then investigate how multiple degrees of freedom can be harnessed to achieve multifunctional optical behavior, thereby aligning with current research trends, and offer a consolidated overview of multifunctional meta-devices.

Keywords: metasurface; phase modulation; polarization optics

1. Introduction

In modern optics and photonic technology, optical devices have been widely used to manipulate different degrees of freedom (DoFs) of light, such as amplitude, wavelength, phase, polarization, and angular momentum. Although optical systems composed of bulky optical elements can stably and effectively generate and control light fields in a complex manner, the trend toward device integration necessitates the simplification of optical systems into ultrathin, compact on-chip devices. Consequently, achieving multi-dimensional manipulation of light fields at the micro-nano scale has become a common challenge in both fundamental and applied disciplines. The emergence of metasurfaces based on the generalized Snell's law has shed light on this problem [1,2]. These structures reveal the propagation behavior at the interfaces of different materials at subwavelength scales, subverting the conventional laws of refraction and reflection. Thus, metasurfaces can achieve complex optical modulation functions through pixelated phase or amplitude modulation at the nanometer scale, advancing the integration of optical devices in principle. Over the decade of metasurface development, this field has gradually formed three fundamental phase mechanisms—resonance phase, geometric phase (Pancharatnam–Berry phase), and propagation phase—leading to the creation of compact devices such as metalenses [3–13], invisibility carpets [14], and metasurface-based quantum light sources [15,16].

However, metasurfaces based on the above phase principles face obstacles in the design and application of multifunctional micro-nano photonic devices. For resonance phase, researchers need to design various microstructures that satisfy the target phase at specific resonant wavelengths, which often suffers from bandwidth limitations [17]. Although the geometric phase is independent of the device's operational wavelength,

Check for updates

Received: 11 March 2026
Revised: 19 March 2026
Accepted: 23 March 2026
Published: 25 March 2026

Copyright: © 2026 by the authors. Licensee MDPI, Basel, Switzerland. This article is an open access article distributed under the terms and conditions of the Creative Commons Attribution (CC BY) license.

its dependence on circularly polarized light and its conjugate chiral relationship prevent independent wavefront control [18,19]. Propagation phase, on the other hand, relies on the phase accumulation of light within the medium, so its modulation capability and device efficiency are related to the height of the medium [20,21]. These non-tunable, single-function metasurfaces cannot meet the demands of multifunctional photonic platforms. Therefore, research into the multifunctionality of metasurfaces has gained significant attention, aiming to achieve multifunctional metasurface devices capable of multi-dimensional light-field manipulation [11,22–41]. Consequently, designing multifunctional metaphotonic devices has become a research hotspot.

In recent years, the proposal of various hybrid and novel phase mechanisms has broken through the above limitations, further widening the gap between metasurfaces and conventional devices in terms of integration. This review focuses on the phase modulation principles of metasurfaces. Based on different physical mechanisms, we first review the three fundamental phases. Then, we analyze the working principles and implementation methods of hybrid phases based on geometric phase combined with resonance or propagation phase, validated by simulation results based on amorphous silicon. Subsequently, several novel phase mechanisms and principles for multifunctional metasurfaces are introduced, including orbit-orbit phase, topological phase metasurfaces. Finally, we summarize and provide an outlook on the future development of multifunctional metaphotonics.

2. Fundamental Phase Mechanism with Typically Single Function

2.1. Resonance Phase Based on Plasmonics

The generalized Snell's law describes the behavior of reflected and refracted light waves at the interface between two different media upon incidence [1]. At the subwavelength scale, when incident light interacts with an interface separating two media with distinct refractive indices, as illustrated in Figure 1a, the optical path difference can be expressed as:

$$k_0 n_i \sin(\theta_i) dx + (\phi + d\phi) = k_0 n_t \sin(\theta_t) dx + \phi \quad (1)$$

This simplifies to:

$$n_t \sin(\theta_t) - n_i \sin(\theta_i) = \frac{\lambda_0}{2\pi} \frac{d\phi}{dx} \quad (2)$$

and for reflective case, we have:

$$k_0 n_i \sin(\theta_i) dx + (\phi + d\phi) = k_0 n_r \sin(\theta_r) dx + \phi \quad (3)$$

which can be reduced to:

$$\sin(\theta_r) - \sin(\theta_i) = \frac{\lambda_0}{2\pi n_i} \frac{d\phi}{dx} \quad (4)$$

Here, $k_0 = 2\pi/\lambda_0$ is the wavevector at the central wavelength λ_0, while n_i, n_t, and n_r denote the refractive indices of the incident, transmissive, and reflective media, respectively. The angles θ_i, θ_t, and θ_r correspond to the incident, transmitted, and reflected angles. The terms ϕ and $d\phi$ represent the phase shifts introduced at the interface along two adjacent optical paths. When $d\phi/dx = 0$, the generalized laws revert to the classical Snell's law.

As shown in the upper panel of Figure 1b, V-shaped gold nanoantennas with dual-resonance characteristics enable complete wavefront control. These subwavelength metallic structures function as optical resonators: when the incident wavelength matches the resonant condition, displacement currents generate a strongly scattered electromagnetic field. During resonance, the phase shift between the scattered and incident fields undergoes significant variation. The electric field components parallel and perpendicular to the symmetry axis of the V-shaped antenna excite symmetric and antisymmetric modes, respectively. By spatially tailoring the geometry of these two-dimensional nanoantenna arrays, the resonant wavelength shifts progressively, achieving phase coverage from 0 to 2π. This allows customizable discontinuous phase profiles along the interface, enabling phenomena such as anomalous refraction/reflection and vortex beam generation. In the microwave regime, the lower panel of Figure 1b depicts H-shaped metastructures that convert surface waves into radiation waves, experimentally validating the generalized Snell's law during the same period [2].

2.2. Pancharatnam–Berry Phase

Next, we introduce another phase mechanism independent of the working bandwidth. In 1956, Indian scientist Pancharatnam discovered that transformations in the polarization state of electromagnetic waves introduce an additional phase shift. Nearly three decades later, Sir Michael V. Berry proposed that a system undergoing an adiabatic cyclic evolution acquires a phase dependent solely on the geometric path traversed in parameter space, and hence it is also called geometric phase. Synthesizing these insights, the geometric phase mechanism can be elegantly understood through the Poincaré sphere (PS) representation of polarization conversion, as illustrated in Figure 1c. When light traverses a closed loop on the PS—from the north pole (left circular polarization, LCP), through the equator, to the south pole (right circular polarization, RCP), and back to the north pole—the accumulated phase equals half the solid angle enclosed by the path. The polarization response of a metasurface can be described by the Jones matrix [42,43]:

$$J = \boldsymbol{R}(-\theta)\begin{bmatrix} t_u & 0 \\ 0 & t_v \end{bmatrix}\boldsymbol{R}(\theta) \tag{5}$$

with rotation matrix labeled as $\boldsymbol{R}(\theta)$:

$$\boldsymbol{R}(\theta) = \begin{bmatrix} cos\theta & sin\theta \\ -sin\theta & cos\theta \end{bmatrix} \tag{6}$$

where $t_{u,v}$ represents the transmissive coefficient along the fast and slow axes of the meta-atom. θ denotes the rotation angle of the anisotropic structure around the reference coordinate. We can further simplify Equation (6) by substituting Equation (7) into it, obtaining:

$$J = \begin{bmatrix} t_u\cos^2\theta + t_v\sin^2\theta & (t_u - t_v)\sin\theta\cos\theta \\ (t_u - t_v)\sin\theta\cos\theta & t_u\sin^2\theta + t_v\cos^2\theta \end{bmatrix} \tag{7}$$

define $E_{x,y}^{in}$ and $E_{x,y}^{out}$ represent the x and y polarization components of the incoming and outgoing electromagnetic waves, respectively. Once circular polarization (CP) incidence, the output light field can be expressed as:

$$\begin{bmatrix} E_x^{out} \\ E_y^{out} \end{bmatrix} = J \begin{bmatrix} 1 \\ i\sigma \end{bmatrix} = \frac{t_u + t_v}{2} \begin{bmatrix} 1 \\ i\sigma \end{bmatrix} + \frac{t_u - t_v}{2} e^{2i\sigma\theta} \begin{bmatrix} 1 \\ -i\sigma \end{bmatrix} \quad (8)$$

Here, $\sigma = \pm 1$ denotes the chirality (handedness) of the incident CP light. The output field retains the original polarization component while generating orthogonally polarized components that carry an additional geometric phase of $2\sigma\theta$. Crucially, the geometric phase depends only on the incident polarization σ and the orientation angle θ of the anisotropic structures, remaining entirely independent of the operational wavelength, as illustrated in Figure 1c. Very recently, metasurfaces based on quasi-bound states in the continuum (qBIC) [44–47], also referred to as nonlocal metasurfaces, have attracted significant interest due to their ability to exhibit optical responses within an extremely narrow bandwidth while remaining inefficient at other wavelengths and demonstrating high Q-factors. These metasurfaces are typically composed of symmetry-broken nanoantenna arrays. Similarly, such qBIC metasurfaces can leverage geometric phases to achieve wavefront modulation with ultra-narrow bandwidths, as illustrated in Figure 1d, where we present three representative examples of geometric phase qBIC metasurfaces from top to bottom [48–50]. With the increasing diversification of nanoantenna designs, further research on geometric phase modulation based on qBIC metasurfaces is expected to emerge.

2.3. Propagation Phase Based on Dielectrics

Metallic metasurfaces utilizing resonance phases suffer from Ohmic losses, limiting their working efficiency. To overcome this limitation, dielectric metasurfaces have attracted considerable attention due to their low-loss characteristics and compatibility with conventional electronic fabrication processes. Common materials include silicon (Si), titanium dioxide (TiO_2), silicon nitride (Si_3N_4), and gallium nitride (GaN). These dielectric metasurfaces achieve phase modulation through the phase accumulated as light propagates through high-aspect-ratio waveguide-type antennas—a mechanism known as propagation phase or dynamic phase, as shown in Figure 1e [51]. For an electromagnetic wave of wavelength λ propagating a distance d through a medium of refractive index n, the accumulated propagation phase is given by [20]:

$$\phi = (2\pi/\lambda)nd \quad (9)$$

Achieving full 2π phase coverage typically requires a substantial thickness d. Since metasurfaces generally maintain uniform structural thickness, phase modulation is accomplished by spatially varying the effective refractive index n of each microstructure, usually through geometric parameter adjustments. Due to the inherent bandwidth of the propagation phase, it can maintain consistent resonance within a certain spectral range, thereby preserving the phase profile. This allows for wavefront modulation at multiple wavelengths by optimizing several specific resonances of the same type of nanoantenna [52–54]. Figure 1f demonstrates the feasibility of this approach [55]. By optimizing the phase distributions at three wavelengths (910 nm, 1064 nm, and 1310 nm), a tri-wavelength multiplexed polarization-independent multifunctional metasurface can be realized, generating focused vortex beam, Bessel beam, and focused Gaussian beam, respectively.

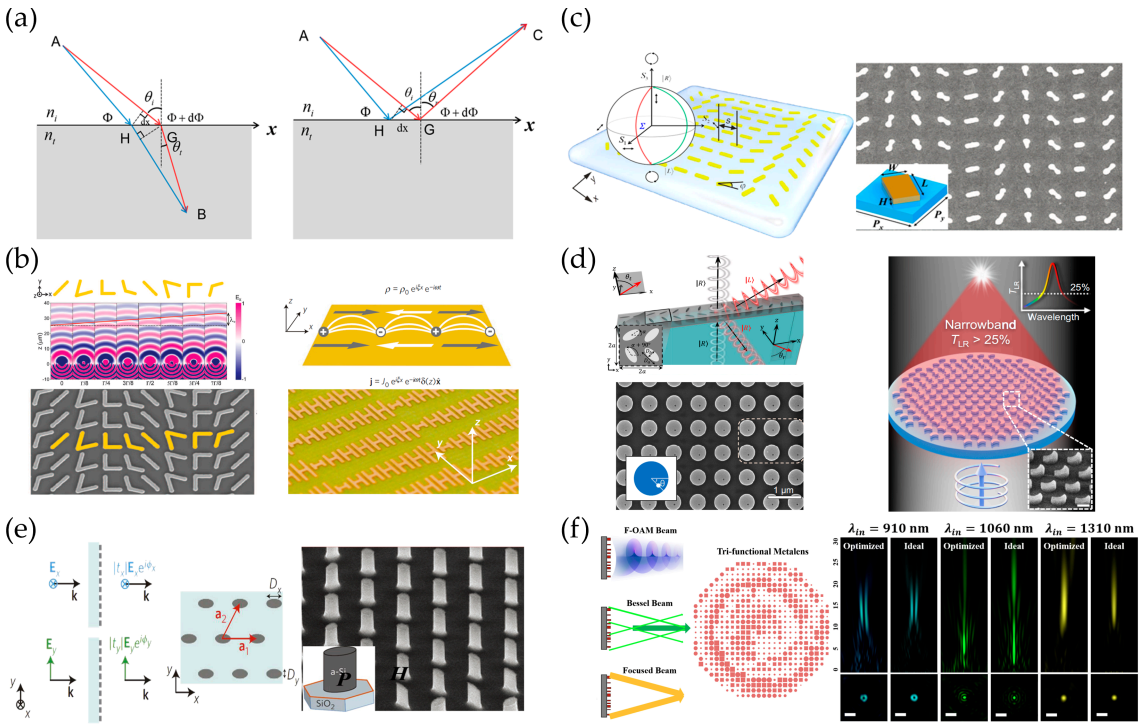


Figure 1. Fundamental phase modulation mechanisms in metasurfaces. (**a**) Generalized Snell's law at an interface [1]. (**b**) V-shaped nanoantennas (upper) and H-shaped microwave structures (lower) validating the generalized law [2]. (**c**) Pancharatnam–Berry geometric phase illustrated via the Poincaré sphere [3,56]. (**d**) Geometric phase metasurfaces based on quasi-bound states in the continuum (qBIC). (**e**) Propagation phase in dielectric waveguide-type antennas [51]. (**f**) A tri-wavelength multifunctional metasurface generating different beams [55].

3. Hybrid Phase Mechanism with Multiple Functions

The fundamental phases introduced above each have their own advantages and limitations in wavefront modulation. However, to achieve multifunctional capabilities, these fundamental phases require further adaptation. Given that the geometric phase operates on a mechanism distinct from the other two fundamental phases, hybrid phase patterns combining resonance with geometric phase or propagation with geometric phase have emerged. Practical applications have demonstrated that these hybrid phases enable simultaneous modulation of multiple optical degrees of freedom, facilitating the design and fabrication of multifunctional optical devices [57]. In the following sections, this article will systematically introduce these multidimensional modulation phase patterns and validate the underlying principles through simulations.

Returning to the Jones matrix in Equation (6), the complex amplitude t_u and t_v can be expressed as $t_u = \mathrm{T}_o e^{\mathrm{i}\varphi \mathrm{o}}$ and $t_v = \mathrm{T}_e e^{\mathrm{i}\varphi \mathrm{e}}$, where o and e represent the ordinary and extraordinary light of each antenna. Assuming that the transmission amplitudes for two orthogonal polarizations are equal—i.e., $T_o = T_e = T$—the Jones matrix can be further simplified based on the incident polarization state. As is well established, light–matter interactions are typically characterized through the response to two fundamental types of polarization states: linear polarization (LP) and CP. Taking these two representative cases as examples, the corresponding Jones matrices can be expressed in the CP basis $[E_R\ E_L]^T$ and the LP basis $[E_H\ E_V]^T$, respectively. Here, the subscripts R and L denote right-handed and left-handed circular polarization states, while H and V represent horizontal and vertical

linear polarization states. Therefore, the matrices applied with two bases can be written as follows [58]:

$$J(LP) = Te^{i\varphi_o}\begin{bmatrix} e^{i\varphi_1} & e^{i\varphi_2} \\ e^{i\varphi_2} & e^{i\varphi_3} \end{bmatrix}, \begin{cases} e^{i\varphi_1} = cos^2\theta e^{i\varphi_o} + sin^2\theta e^{i\varphi_e} \\ e^{i\varphi_2} = cos\theta sin\theta e^{i\varphi_e} - cos\theta sin\theta e^{i\varphi_o} \\ e^{i\varphi_3} = cos^2\theta e^{i\varphi_e} + sin^2\theta e^{i\varphi_o} \end{cases} \quad (10)$$

$$J(CP) = Te^{i\varphi_o}\begin{bmatrix} \cos\left(\frac{\delta}{2}\right) & isin(\delta/2)e^{-i2\theta} \\ isin(\delta/2)e^{i2\theta} & \cos\left(\frac{\delta}{2}\right) \end{bmatrix} \quad (11)$$

where $\delta = \phi_o - \phi_e$ represents the phase retardation, and $\phi_0 = (\phi_o + \phi_e)/2$ denotes the propagation phase contributed by the ordinary and extraordinary components, respectively.

The Jones matrices presented above do not directly reveal the underlying dimensions that can be modulated. To establish clearer modulation principles, we further examine the total output fields, which consist of a superposition of different polarization states, as schematically illustrated in Figure 3a,b. For incidence in the form of LP, specifically the $|H\rangle$ or $|V\rangle$ state, the resulting output field takes the form $[e^{i\varphi 1}\ e^{i\varphi 2}]^T$ or $[e^{i\varphi 3}\ e^{i\varphi 4}]^T$, respectively. To establish a more general framework, we consider the superposition state of $|H\rangle$ and $|V\rangle$—namely, the $|D\rangle$ state—as a representative case (Figure 2a). In this context, the output vector field can be further expressed as:

$$E_{out}^{LP} = Te^{i\varphi_1}\Big|H\rangle + Te^{i\varphi_2}\Big|D\rangle + Te^{i\varphi_3}\Big|V\rangle \quad (12)$$

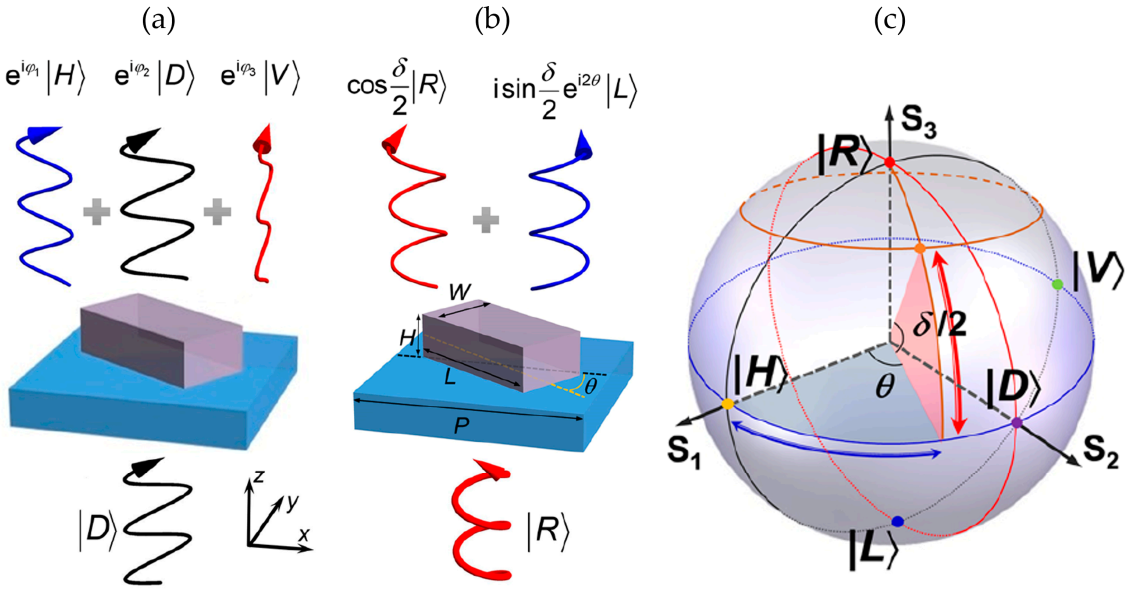


Figure 2. The hybrid phase mechanism integrates both geometric and propagation phases. Figures (**a**) and (**b**) illustrate the transmission characteristics of a meta-atom corresponding to two distinct polarization bases. (**c**) depicts the conversion of polarization states on the Poincaré sphere [58].

For incidence in the $|R\rangle$ state, the output field naturally decomposes into two orthogonally polarized components: the co-polarized and cross-polarized components (Figure 2b). Accordingly, the output vector field can be expressed as:

$$E_{out}^{CP} = Te^{i\varphi_o}\cos(\delta/2)\Big|R\rangle + iTe^{i\varphi_o}\sin(\delta/2)e^{i2\theta}\Big|L\rangle \quad (13)$$

The modulation process arising from the conversion of polarization states on the PS is illustrated in Figure 2c. Evidently, the equations above provide intuitively accessible

parameter dimensions for modulation, encompassing amplitude, phase, and polarization. As described by Equation (6), meta-atoms can be conceptualized as waveplates capable of achieving arbitrary phase retardation (δ) through engineered birefringence. This phase retardation further leads to complementary intensities between the two orthogonal circularly polarized components. Leveraging this principle, various functional devices have been demonstrated, including polarization transformers and ultrathin beam splitters with tailorable energy distributions. Notably, this type of modulation—whether applied to amplitude or polarization—involves only a single degree of freedom in control.

The hybrid phase mechanism has enabled a wide range of multifunctional photonic applications. For instance, in imaging applications, hybrid phase metasurfaces have demonstrated polarization-multiplexed metalenses capable of projecting different focal spots or images depending on the incident polarization state [59–61]. In holography, researchers have achieved independent holograms under orthogonal polarization channels, effectively doubling the information capacity within a single device [62,63]. Furthermore, structured light generation represents another thriving application area by using such metasurfaces to generate customizable vector vortex beams with tailored polarization and phase profiles [18,64]. Beyond these, optical micromanipulation has also benefited from hybrid phase designs, where spin-dependent optical forces enable simultaneous trapping and rotation of microscopic particles—functionalities that traditionally required complex bulk optical setups [26,65]. These diverse applications collectively demonstrate that hybrid phase modulation serves as a versatile platform for integrating multiple optical functions into ultrathin devices.

While hybrid phase mechanisms have enabled remarkable multifunctional capabilities, fundamental physical trade-offs emerge as more functions are integrated. First, efficiency inevitably degrades with increasing functionality, as each multiplexed DoF partitions the available electromagnetic energy among multiple output channels. For example, in polarization-multiplexed designs based on Equation (14), the cross-polarized conversion efficiency is fundamentally limited to $\sin^2(\delta/2)$—a direct consequence of energy conservation rather than a technical limitation that can be optimized away. Second, inter-channel crosstalk arises from multiple sources: fabrication imperfections introduce unintended phase errors; material dispersion causes wavelength-dependent deviations from target responses; and near-field coupling between densely packed meta-atoms perturbs the idealized isolated-element responses assumed in design. These effects collectively impose practical limits on the number of reliably multiplexed functions. These limitations are ultimately rooted in the finite DoF available in electromagnetic scattering: each meta-atom's adjustable parameters (geometry, orientation, dimensions) must simultaneously satisfy multiple phase and amplitude constraints, analogous to information-theoretic capacity limits.

4. Detour Phase

Detour phase offers a geometric approach to wavefront engineering that originates from computer-generated holography and has been successfully adapted to metasurface platforms, enabling precise phase control through the spatial arrangement of identical meta-atoms rather than modifications to their individual geometry or material composition.

As illustrated in Figure 3a, this mechanism can be understood by examining a metasurface composed of periodic unit cells each containing two identical meta-atoms with controlled positional offsets: when a plane wave of wavelength λ illuminates the structure

at an incident angle $\theta = (\theta_x, \theta_y)$, the complex amplitude distribution at the metasurface plane takes the form as follows [66,67]:

$$U(x,y) = U_0\left(t_1 + t_2 \exp\left(ik_x x + ik_y y\right)\right) \tag{14}$$

where t_1 and t_2 represent the transmission coefficients of the two meta-atoms and $k_{x,y} = k_0 \sin(\theta_{x,y})$ with $k_0 = 2\pi n/\lambda$. For the specific illumination condition $\theta = (\theta_x, \theta_y) = [\sin^{-1}(\lambda/nP), 0]$ corresponding to the first-order diffraction angle, this expression simplifies to:

$$U(x) = U_0 t_2 \exp\left(\frac{i2\pi x}{P}\right) \tag{15}$$

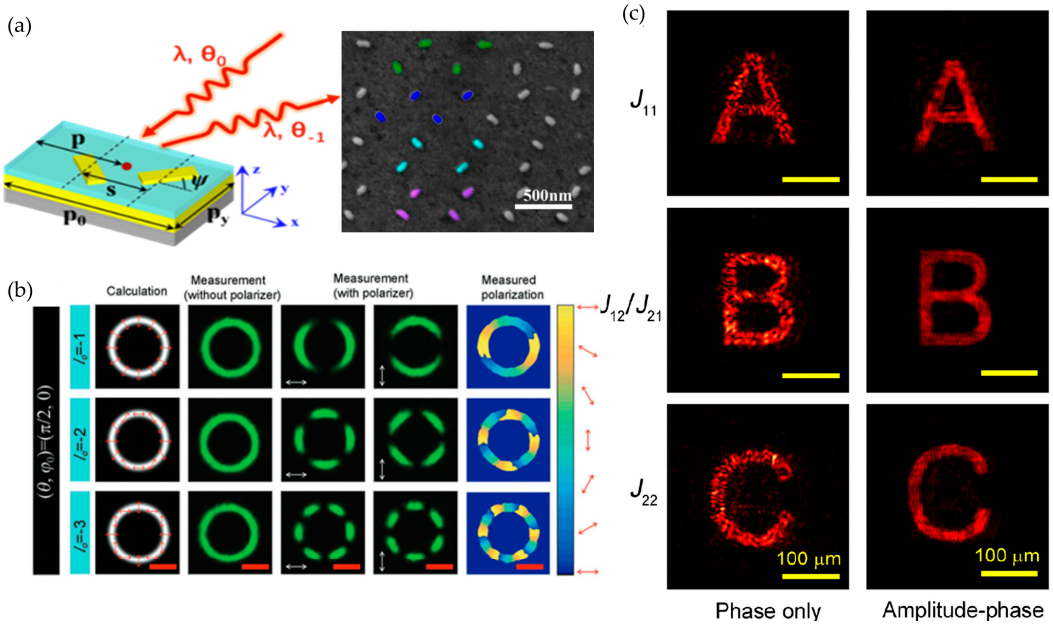


Figure 3. Detour phase metasurfaces. (**a**) Schematic of the detour phase principle. Under first-order diffraction condition, the phase shift $\Delta\varphi = 2\pi\Delta x/P$ depends linearly on the meta-atom displacement Δx within each unit cell [66]. (**b**) Generation of vector light fields with topological charges of -1, -2, and -3 (top to bottom), showing calculated, simulated, and measured results [68]. (**c**) Hologram generation via pure phase and complex amplitude modulation through three Jones matrix channels [69].

This reveals a pure phase gradient along the x-direction. The key insight lies in the relationship between meta-atom displacement and the acquired phase shift: if adjacent nanocolumns within the metasurface are separated by a distance Δx along the x-direction, the waves scattered from these two elements accumulate a relative phase delay $\Delta\varphi = 2\pi\Delta x/P$, known as the detour phase, which depends linearly on the displacement magnitude relative to the grating period P. This geometric origin distinguishes detour phase from resonance-based mechanisms—it operates independently of the specific resonant properties of individual scatterers, relying instead on their precise spatial positioning within each unit cell. From a practical standpoint, this linear relationship between displacement and phase shift enables straightforward implementation of complex phase distributions including spiral phases for vortex beam generation and hyperbolic profiles for metalens focusing, while the decoupling of phase control from meta-atom geometry allows the same nanostructure to serve as a building block for various phase profiles simply by adjusting its position. Figure 3b,c illustrate the potential of the detour phase in multifunctional light field modulation [68,69]. Specifically, Figure 3b demonstrates the generation of vector light

fields, presenting the calculated, simulated, and measured results of intensity distributions and polarization states for topological charges of -1, -2, and -3 from top to bottom. Figure 3c showcases the generation of holograms with pure phase and complex amplitude modulation achieved through three channels of the diagonal elements of the Jones matrix.

5. Exceptional Topological Phase

Topological photonics has rapidly emerged as a transformative research field that employs geometric and topological concepts to fundamentally control light behavior. Unlike conventional photonic approaches that rely on gradual refractive index variations, topological photonics draws inspiration from condensed matter physics—particularly the quantum Hall effect and topological insulators—to create light states that are inherently robust against perturbations and fabrication imperfections [70–73]. These platforms have successfully demonstrated phenomena such as topologically protected edge states and unidirectional waveguides. However, demonstrations of topological phenomena using metasurfaces—two-dimensional planar structures with subwavelength thickness—remain relatively scarce, despite their inherent advantages in compactness, integrability, and multifunctional wavefront control.

In 2021, Song and colleagues made a significant breakthrough by introducing an exceptional topological (ET) phase derived from the topological characteristics of non-Hermitian matrices when encircling exceptional points (EPs) [74]. Exceptional points are singularities in non-Hermitian systems where both eigenvalues and their corresponding eigenvectors coalesce, exhibiting exotic optical behavior distinct from conventional degeneracies. By employing two orthogonally oriented metal rods to induce strong coupling between resonant modes, the researchers engineered metasurface building blocks capable of encircling an exceptional point along arbitrary closed trajectories in parameter space. This topological encircling process enabled the accumulation of a geometric phase that is non-trivial and topologically protected, yielding a full 2π phase coverage within a designated reflective polarization channel, as shown in Figure 4a. Notably, unlike conventional geometric phase (Pancharatnam–Berry phase) which exhibits conjugate phase relationships between orthogonal circular polarizations, the ET phase accumulation selectively targets only one of the two circularly polarized states defined by the chirality direction when encircling the exceptional point—a fundamental distinction that breaks the conventional phase conjugation symmetry. Unlike photonic topological insulators, whose topological properties arise from bulk-boundary correspondence and manifest as robustness against defects, the topological characteristics of the exceptional phase originate from the non-Hermitian topology of the Jones matrix eigenvalues under circularly polarized incidence, manifested in the complex plane.

The researchers demonstrated that ET phase and geometric phase mechanisms can operate synergistically within the same metasurface platform, enabling independent and complete control over multiple polarization channels without mutual interference, as illustrated in Figure 4b. This orthogonality between phase mechanisms arises because ET phase originates from non-Hermitian topological effects while geometric phase stems from polarization path dependence on the Poincaré sphere—two physically distinct origins that can be independently engineered. Validation experiments confirmed optical holographic multiplexing where distinct information was independently encoded onto different circularly polarized output beams, successfully incorporating geometric phase contributions alongside ET phase control, as depicted in Figure 4c. Furthermore, by judiciously combining multiple meta-atoms with tailored ET and geometric phase responses, the team achieved multidimensional holographic multiplexing under various polarization incidences. Diverse and switchable holographic patterns were generated through controlled interference

among ET meta-atoms arranged in supercell structures, as presented in Figure 4d [75], demonstrating the potential for high-capacity optical information encoding.

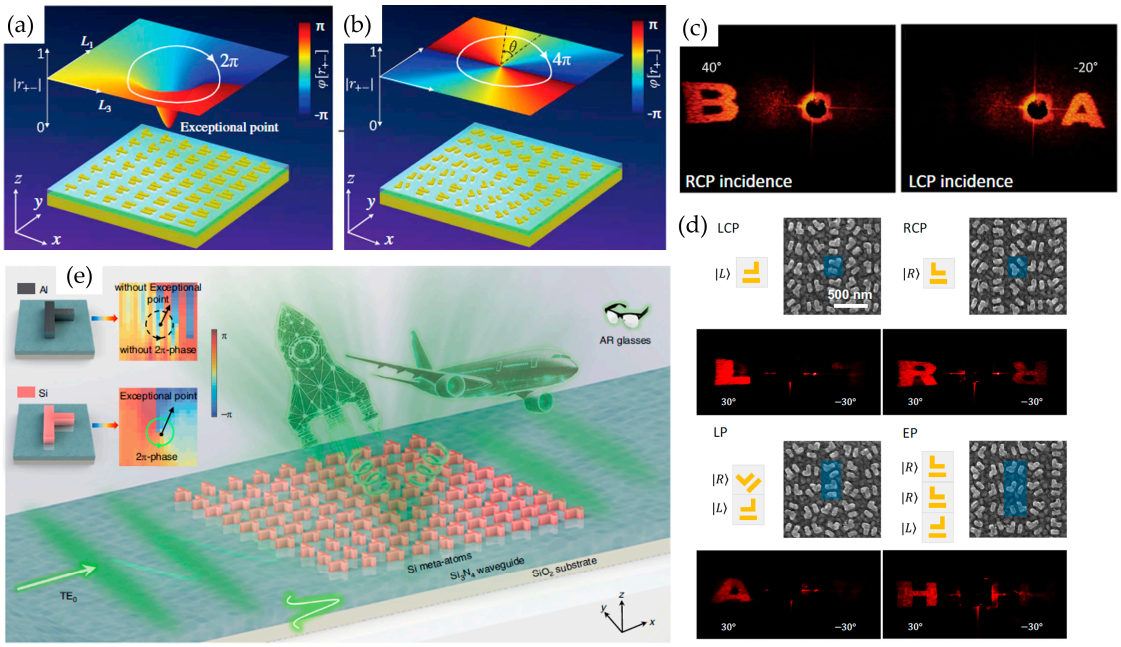


Figure 4. Exceptional topological (ET) phase metasurfaces. (**a**) ET phase mechanism enabling 2π phase coverage in a reflective polarization channel by encircling exceptional points [74]. (**b**) Synergistic operation of ET phase and geometric phase within the same metasurface, allowing independent control over multiple polarization channels [74]. (**c**) Holographic multiplexing demonstration with independent information encoded onto different circularly polarized outputs [74]. (**d**) Multidimensional holographic multiplexing achieved by combining multiple ET meta-atoms in supercell structures [75]. (**e**) Waveguide-integrated ET phase holography for far-field projections, showing potential for augmented reality (AR) glass applications [76].

A particularly compelling extension of this work involved waveguide-integrated ET phase holography, as shown in Figure 4e [76], where guided waves interacting with the metasurface excited ET phase responses to generate far-field holographic projections. This configuration eliminates free-space optical alignment complexities and offers seamless integration with planar photonic circuits. The waveguide-integrated approach holds particular promise for augmented reality (AR) glass technology, where compact form factors, lightweight construction, and efficient light coupling are essential requirements. By combining ET phase holography with waveguide architectures, it becomes possible to project complex, polarization-multiplexed virtual images directly into the user's field of view while maintaining the thin profile necessary for wearable displays.

6. Conclusions

This review elucidates the fundamental design principles underlying multidimensional multiplexing in multifunctional metasurfaces. It demonstrates that multifunctional metadevices employing hybrid phases—specifically, combinations of geometric phase with either propagation or resonance phase—not only achieve enhanced functional integration but also facilitate independent development along two orthogonal dimensions: polarization control and wavelength manipulation. Furthermore, the detour phase mechanism—which enables diffracted wavefront modulation through simultaneous control of nanopillar spacing and orientation—is discussed. Similarly, exceptional topological (ET) phase engineered in parameter space can be combined with geometric phase to realize polarization-decoupled

functionality. These collective efforts establish that multifunctional metasurface phase mechanisms necessitate the integration of non-interfering phase modes. We conclude all the mechanisms in this paper as shown in Table 1.

Table 1. Comparison of discussed phase mechanisms.

Reference	Phase Type	Geometric Variables	Multiplexing Capacity	Bandwidth
[1,2]	Resonance phase	φ_0	1	Resonant bandwidth
[3,4,15,38,45,46] [48–50,56]	Pancharatnam–Berry phase	θ	1	Broadband
[16,17,20,27,36,51,52,55]	Propagation phase	φ_0	1, 2	Limited bandwidth
[7,18,19,22,24,26,28,34] [59–65]	Hybrid phase	φ_e, φ_0, θ	2, 3	Limited bandwidth
[66–69]	Detour phase	Δx, θ	2, 3	Limited bandwidth
[74–76]	Exceptional topological phase	φ_0	1	Narrow bandwidth

Compared to traditional bulk optical assemblies, multifunctional metasurfaces offer dramatic advantages in form factors (thickness < λ), integration density, and weight reduction, while simultaneously eliminating the alignment tolerances required between discrete optical components. To further manipulate more channels, multilayer metasurfaces introduce additional design DoFs by enabling superposition of Jones matrices or phase masks. For instance, bilayer metasurfaces can achieve at most 8 independent channels [77,78], which has emerged as a promising route toward actively tunable multifunctional devices.

As the demand for multifunctional metasurfaces continues to escalate, the advent of novel phase modulation mechanisms has undeniably accelerated progress in metaphotonics. Contemporary metasurface research increasingly emphasizes practical implementation, with future trajectories collectively shaped by three critical metrics: modulation dimensionality, operational efficiency, and device robustness. Efficiency predominantly depends on microstructural geometric parameters and judicious material selection tailored to target wavelength bands. Meanwhile, modulation dimensionality and robustness are intrinsically governed by underlying physical mechanisms. We anticipate the emergence of additional phase modulation paradigms that will expand the design DoFs available to metasurface engineers. Concurrently, we envision the realization of a new generation of high-efficiency, tunable multifunctional integrated devices leveraging these phase mechanisms—advancements poised to propel micro-nano applied photonics into its next phase of development.

The practical translation of multifunctional metasurfaces from laboratory concepts to commercial products critically depends on scalable fabrication techniques. Electron-beam lithography (EBL) offers the highest resolution essential for visible-light metasurfaces but suffers from low throughput and high cost, limiting its use to research prototyping [79,80]. Nano-imprint lithography (NIL) provides a high-throughput alternative capable of replicating nanostructures with sub-10 nm fidelity across large areas, though it requires defect-free master molds typically fabricated by EBL. CMOS-compatible deep-ultraviolet (DUV) lithography leverages existing semiconductor infrastructure for mass production but faces resolution constraints that restrict its applicability for shorter visible wavelengths. The optimal choice among these techniques involves balancing resolution, throughput, and cost according to specific application requirements.

Beyond fabrication scalability, another critical challenge lies in transitioning from static multifunctional devices to actively tunable/reconfigurable metasurfaces [81,82]. Current approaches include integrating phase-change materials that exploit refractive index

contrast between amorphous and crystalline states, though cyclability and switching energy remain concerns. Liquid crystal integration offers electrical addressability with lower power consumption but faces speed and alignment challenges. Emerging MEMS-based approaches enable mechanical reconfiguration at the cost of increased complexity. The convergence of static multiplexing with active tuning mechanisms represents a promising direction for future research.

Looking forward, the trajectory of metasurface technology is firmly set towards exploiting its most profound advantage: the ability to replace bulky conventional optical components with planar, lightweight alternatives. This intrinsic capacity for extreme miniaturization and mass reduction will be the primary driver for its integration into future technologies. We can anticipate a paradigm shift where the heavy lens assemblies of contemporary augmented reality headsets are supplanted by nearly transparent, flat metasurfaces, enabling truly glasses-like form factors. Beyond consumer electronics, this leap in weight reduction will unlock unprecedented capabilities in aerospace and automotive sectors; for instance, deploying fleets of lightweight, high-resolution metasurface-based LiDAR on drones and satellites for autonomous navigation and Earth observation [83,84], where every gram of payload impacts fuel efficiency and launch costs. Furthermore, in the biomedical field, the reduced footprint of metasurface-enabled endoscopes and microscopes will facilitate less invasive procedures and point-of-care diagnostic tools.

Author Contributions: Conceptualization, A.L.; writing—original draft preparation, A.L.; writing—review and editing, Z.B., Z.X. and X.W.; visualization, A.L.; supervision, A.L.; project administration, A.L.; funding acquisition, A.L. All authors have read and agreed to the published version of the manuscript.

Funding: This research was funded by the Natural Science Foundation of Shandong Province (ZR2024QB388) and the Foundation of Yantai Vocational College (2021005).

Informed Consent Statement: Informed consent was obtained from all subjects involved in the study.

Data Availability Statement: No new data was created.

Acknowledgments: The authors thank the help from Boheng Zhang 's support.

Conflicts of Interest: The authors declare no conflicts of interest.

References

1. Yu, N.; Genevet, P.; Kats, M.A.; Aieta, F.; Tetienne, J.-P.; Capasso, F.; Gaburro, Z. Light propagation with phase discontinuities: Generalized laws of reflection and refraction. *Science* **2011**, *334*, 333–337. [CrossRef]
2. Sun, S.; He, Q.; Xiao, S.; Xu, Q.; Li, X.; Zhou, L. Gradient-index meta-surfaces as a bridge linking propagating waves and surface waves. *Nat. Mater.* **2012**, *11*, 426–431. [CrossRef] [PubMed]
3. Chen, X.; Huang, L.; Mühlenbernd, H.; Li, G.; Bai, B.; Tan, Q.; Jin, G.; Qiu, C.-W.; Zhang, S.; Zentgraf, T. Dual-polarity plasmonic metalens for visible light. *Nat. Commun.* **2012**, *3*, 1198. [CrossRef]
4. Chen, X.; Chen, M.; Mehmood, M.Q.; Wen, D.; Yue, F.; Qiu, C.W.; Zhang, S. Longitudinal multifoci metalens for circularly polarized light. *Adv. Opt. Mater.* **2015**, *3*, 1201–1206. [CrossRef]
5. Khorasaninejad, M.; Chen, W.T.; Devlin, R.C.; Oh, J.; Zhu, A.Y.; Capasso, F. Metalenses at visible wavelengths: Diffraction-limited focusing and subwavelength resolution imaging. *Science* **2016**, *352*, 1190–1194. [CrossRef]
6. Wang, S.; Wu, P.C.; Su, V.-C.; Lai, Y.-C.; Hung Chu, C.; Chen, J.-W.; Lu, S.-H.; Chen, J.; Xu, B.; Kuan, C.-H. Broadband achromatic optical metasurface devices. *Nat. Commun.* **2017**, *8*, 187. [CrossRef]
7. Fan, Q.; Wang, Y.; Liu, M.; Xu, T. High-efficiency, linear-polarization-multiplexing metalens for long-wavelength infrared light. *Opt. Lett.* **2018**, *43*, 6005–6008. [CrossRef] [PubMed]
8. Wang, S.; Wu, P.C.; Su, V.-C.; Lai, Y.-C.; Chen, M.-K.; Kuo, H.Y.; Chen, B.H.; Chen, Y.H.; Huang, T.-T.; Wang, J.-H. A broadband achromatic metalens in the visible. *Nat. Nanotechnol.* **2018**, *13*, 227–232. [CrossRef]

9. Fu, B.; Bi, Q.; Zheng, S.; Peng, Y.; Wang, S.; Cao, X.; Wang, Z.; Zhu, S. Advanced Metasurface Imaging and Display Based on Multidimensional Light Field Manipulation (Invited). *Acta Opt. Sin.* **2024**, *44*, 1400001.
10. Zheng, S.; Yu, Y.; Zhou, X.; Fu, B.; Wang, S.; Wang, Z.; Zhu, S. Research on Multidimensional Optical Imaging Empowered by Metasurfaces (Invited). *Laser Optoelectron. Prog.* **2024**, *61*, 1611001.
11. Sun, Z.; Li, T.; Kuang, S.; Yun, X.; He, M.; Fu, B.; Fu, Y.; Zhao, T.; Wang, S.; Liang, Y. On-demand quick metasurface design with neighborhood attention transformer. *arXiv* **2024**, arXiv:2412.08405. [CrossRef]
12. Lin, R.; Wu, Y.; Fu, B. Application of chromatic aberration control of metalens. *Chin. Opt.* **2021**, *14*, 764–781. [CrossRef]
13. Fu, B.; Zou, X.; Li, T.; Wang, S.; Wang, Z.; Zhu, S. Chromatic Dispersion Manipulation Based on Optical Metasurfaces. *J. Harbin Inst. Technol. (New Ser.)* **2020**, *27*, 1–19.
14. Ni, X.; Wong, Z.J.; Mrejen, M.; Wang, Y.; Zhang, X. An ultrathin invisibility skin cloak for visible light. *Science* **2015**, *349*, 1310–1314. [CrossRef]
15. Bao, Y.; Lin, Q.; Su, R.; Zhou, Z.-K.; Song, J.; Li, J.; Wang, X.-H. On-demand spin-state manipulation of single-photon emission from quantum dot integrated with metasurface. *Sci. Adv.* **2020**, *6*, eaba8761. [CrossRef]
16. Li, L.; Liu, Z.; Ren, X.; Wang, S.; Su, V.-C.; Chen, M.-K.; Chu, C.H.; Kuo, H.Y.; Liu, B.; Zang, W. Metalens-array–based high-dimensional and multiphoton quantum source. *Science* **2020**, *368*, 1487–1490. [CrossRef]
17. Nazemosadat, E.; Mazur, M.; Kruk, S.; Kravchenko, I.; Carpenter, J.; Schröder, J.; Andrekson, P.A.; Karlsson, M.; Kivshar, Y. Dielectric broadband metasurfaces for fiber mode-multiplexed communications. *Adv. Opt. Mater.* **2019**, *7*, 1801679. [CrossRef]
18. Devlin, R.C.; Ambrosio, A.; Rubin, N.A.; Mueller, J.B.; Capasso, F. Arbitrary spin-to–orbital angular momentum conversion of light. *Science* **2017**, *358*, 896–901. [CrossRef]
19. Balthasar Mueller, J.; Rubin, N.A.; Devlin, R.C.; Groever, B.; Capasso, F. Metasurface polarization optics: Independent phase control of arbitrary orthogonal states of polarization. *Phys. Rev. Lett.* **2017**, *118*, 113901. [CrossRef]
20. Khorasaninejad, M.; Zhu, A.Y.; Roques-Carmes, C.; Chen, W.T.; Oh, J.; Mishra, I.; Devlin, R.C.; Capasso, F. Polarization-insensitive metalenses at visible wavelengths. *Nano Lett.* **2016**, *16*, 7229–7234. [CrossRef]
21. Zou, X.; Gong, G.; Lin, Y.; Fu, B.; Wang, S.; Zhu, S.; Wang, Z. Metasurface-based polarization color routers. *Opt. Lasers Eng.* **2023**, *163*, 107472. [CrossRef]
22. Li, T.; Gao, W.; Fu, B.; Shao, T.; Fu, Y.; Zavatski, S.; Nayak, J.K.; Yan, S.; Xu, X.; Wang, S. Scalable Generalized Meta-Spanners Enabling Parallel Multitasking Optical Manipulation. *Sci. Adv.* **2026**, *12*, eaed5302.
23. Li, T.; Fu, B.; Ren, J.; Wang, S.; Wang, Z.; Zhu, S. Multidimensional light field manipulation and applications based on optical metasurface. In *Proceedings of First Optics Frontier Conference*; SPIE: Bellingham, WA, USA, 2021; p. 1185004.
24. Li, T.; Li, X.; Yan, S.; Xu, X.; Wang, S.; Yao, B.; Wang, Z.; Zhu, S. Generation and conversion dynamics of dual Bessel beams with a photonic spin-dependent dielectric metasurface. *Phys. Rev. Appl.* **2021**, *15*, 014059. [CrossRef]
25. Xu, X.; Gao, W.; Li, T.; Shao, T.; Li, X.; Zhou, Y.; Gao, G.; Wang, G.; Yan, S.; Wang, S. Metasurfaces-empowered optical micromanipulation (Invited). *Acta Opt. Sin.* **2024**, *44*, 0500001.
26. Li, T.; Xu, X.; Fu, B.; Wang, S.; Li, B.; Wang, Z.; Zhu, S. Integrating the optical tweezers and spanner onto an individual single-layer metasurface. *Photonics Res.* **2021**, *9*, 1062–1068. [CrossRef]
27. Li, T.; Kingsley-Smith, J.J.; Hu, Y.; Xu, X.; Yan, S.; Wang, S.; Yao, B.; Wang, Z.; Zhu, S. Reversible lateral optical force on phase-gradient metasurfaces for full control of metavehicles. *Opt. Lett.* **2023**, *48*, 255–258. [CrossRef]
28. Li, T.; Liu, M.; Chen, C.; Li, X.; Hou, J.; Yang, X.; Wang, S.; Zhu, S. Realization of spinful metaphotonic stokes skyrmions. *J. Opt.* **2024**, *26*, 09LT01. [CrossRef]
29. Li, T.; Chen, Y.; Fu, B.; Liu, M.; Wang, J.; Gao, H.; Wang, S.; Zhu, S. Spin-Selective Trifunctional Metasurfaces for Deforming Versatile Nondiffractive Beams along the Optical Trajectory. *Laser Photonics Rev.* **2024**, *18*, 2301372. [CrossRef]
30. Li, T.; Liu, M.; Hou, J.; Yang, X.; Wang, S.; Wang, S.; Zhu, S.; Tsai, D.P.; Wang, Z. Chip-scale metaphotonic singularities: Topological, dynamical, and practical aspects. *Chip* **2024**, *3*, 100109. [CrossRef]
31. Li, T.; Xu, H.; Panmai, M.; Shao, T.; Gao, G.; Xu, F.; Hu, G.; Wang, S.; Wang, Z.; Zhu, S. Ultrafast metaphotonics. *Ultrafast Sci.* **2024**, *4*, 0074. [CrossRef]
32. Zhou, Y.; Zhu, X.; Li, T.; Zhou, Z.; Bi, Q.; Liu, J.; Chen, J.; Fu, B.; He, J.; Feng, X. Metasurface-assisted multimodal quantum imaging. *Proc. Natl. Acad. Sci. USA* **2025**, *122*, e2500760122. [CrossRef]
33. Gao, G.; Shao, T.; Li, T.; Wang, S. Harnessing optical forces with advanced nanophotonic structures: Principles and applications. *Discov. Nano* **2025**, *20*, 76. [CrossRef]
34. Fu, B.; Zhou, X.; Li, T.; Zhu, H.; Liu, Z.; Zheng, S.; Zhou, Y.; Yu, Y.; Cao, X.; Wang, S. Miniaturized high-efficiency snapshot polarimetric stereoscopic imaging. *Optica* **2025**, *12*, 391–398. [CrossRef]
35. Zhang, Y.; Li, T.; Wang, S.; Wang, Z.; Zhu, S. Polarization-Dependent Optical Forces Arising from Fano Interference. *Adv. Phys. Res.* **2023**, *2*, 2200048. [CrossRef]
36. Xu, H.; Li, T.; Gao, G.; Fang, S.; Liu, H.; Ding, H.; Chen, X.; Xiong, Y.; Wang, S.; Xu, F. Metasurface-Integrated Pattern-Preserved Fiber Mode Separator. *Adv. Funct. Mater.* **2025**, *35*, 2505081. [CrossRef]

37. Zhang, J.C.; Yao, J.; Tsai, D.P. Meta-lens based on multi-level phase-change. *J. Appl. Phys.* **2024**, *136*, 053101. [CrossRef]
38. Qiu, X.; Zhang, J.; Fan, Y.; Zhou, J.; Chen, L.; Tsai, D.P. Metasurface enabled high-order differentiator. *Nat. Commun.* **2025**, *16*, 2437. [CrossRef]
39. Zhang, J.C.; Chen, M.K.; Liang, Y.; Hong, X.; Wang, M.; Cheng, Y.; Liu, X.; Tsai, D.P.; Pang, S.W. Nanoimprint meta-device for chiral imaging. *Adv. Funct. Mater.* **2023**, *33*, 2306422. [CrossRef]
40. Zhang, J.C.; Chen, M.K.; Fan, Y.; Chen, Q.; Chen, S.; Yao, J.; Liu, X.; Xiao, S.; Tsai, D.P. Miniature tunable Airy beam optical meta-device. *Opto-Electron. Adv.* **2024**, *7*, 230171. [CrossRef]
41. Zhang, J.C.; Wu, G.-B.; Chen, M.K.; Liu, X.; Chan, K.F.; Tsai, D.P.; Chan, C.H. A 6G meta-device for 3D varifocal. *Sci. Adv.* **2023**, *9*, eadf8478. [CrossRef]
42. Yu, N.; Capasso, F. Flat optics with designer metasurfaces. *Nat. Mater.* **2014**, *13*, 139–150. [CrossRef]
43. Chen, H.-T.; Taylor, A.J.; Yu, N. A review of metasurfaces: Physics and applications. *Rep. Prog. Phys.* **2016**, *79*, 076401. [CrossRef]
44. Hsu, C.W.; Zhen, B.; Stone, A.D.; Joannopoulos, J.D.; Soljačić, M. Bound states in the continuum. *Nat. Rev. Mater.* **2016**, *1*, 16048. [CrossRef]
45. Chen, R.; Li, T.; Bi, Q.; Wang, S.; Zhu, S.; Wang, Z. Quasi-bound states in the continuum-based switchable light-field manipulator. *Opt. Mater. Express* **2022**, *12*, 1232–1241. [CrossRef]
46. Chen, R.; Bi, Q.; Li, T.; Wang, S.; Zhu, S.; Wang, Z. Dual-wavelength chiral metasurfaces based on quasi-bound states in the continuum. *J. Opt.* **2023**, *25*, 045001. [CrossRef]
47. Zhang, J.C.; Tsai, D.P.; Pang, S.W. Non-local bound states in the continuum for nanoscale alignment. *Nat. Photonics* **2026**, *20*, 296–300. [CrossRef]
48. Overvig, A.C.; Malek, S.C.; Yu, N. Multifunctional nonlocal metasurfaces. *Phys. Rev. Lett.* **2020**, *125*, 017402. [CrossRef]
49. Yao, J.; Lai, F.; Fan, Y.; Wang, Y.; Huang, S.-H.; Leng, B.; Liang, Y.; Lin, R.; Chen, S.; Chen, M.K. Nonlocal meta-lens with Huygens' bound states in the continuum. *Nat. Commun.* **2024**, *15*, 6543. [CrossRef]
50. Ouyang, X.; Zeng, Y.; Wang, Z.; Bo, B.; Lai, F.; Zhang, C.; Qiu, C.-w.; Song, Q.; Yu, S.; Kivshar, Y. Ultra narrowband geometric-phase resonant metasurfaces. *Proc. Natl. Acad. Sci. USA* **2025**, *122*, e2420830122. [CrossRef]
51. Arbabi, A.; Horie, Y.; Bagheri, M.; Faraon, A. Dielectric metasurfaces for complete control of phase and polarization with subwavelength spatial resolution and high transmission. *Nat. Nanotechnol.* **2015**, *10*, 937–943. [CrossRef]
52. Shi, Z.; Khorasaninejad, M.; Huang, Y.-W.; Roques-Carmes, C.; Zhu, A.Y.; Chen, W.T.; Sanjeev, V.; Ding, Z.-W.; Tamagnone, M.; Chaudhary, K. Single-layer metasurface with controllable multiwavelength functions. *Nano Lett.* **2018**, *18*, 2420–2427. [CrossRef]
53. Yoon, G.; Kim, J.; Mun, J.; Lee, D.; Nam, K.T.; Rho, J. Wavelength-decoupled geometric metasurfaces by arbitrary dispersion control. *Commun. Phys.* **2019**, *2*, 129. [CrossRef]
54. Sisler, J.; Chen, W.T.; Zhu, A.Y.; Capasso, F. Controlling dispersion in multifunctional metasurfaces. *APL Photonics* **2020**, *5*, 056107. [CrossRef]
55. Ren, J.; Li, T.; Fu, B.; Wang, S.; Wang, Z.; Zhu, S. Wavelength-dependent multifunctional metalens devices via genetic optimization. *Opt. Mater. Express* **2021**, *11*, 3908–3916. [CrossRef]
56. Huang, L.; Chen, X.; Muhlenbernd, H.; Li, G.; Bai, B.; Tan, Q.; Jin, G.; Zentgraf, T.; Zhang, S. Dispersionless phase discontinuities for controlling light propagation. *Nano Lett.* **2012**, *12*, 5750–5755. [CrossRef]
57. Liu, M.; Li, T.; Ge, Q.; Wang, S.; Wang, Z.; Zhu, S. Phase modulation mechanism and research progress of multifunctional metasurfaces. *Acta Opt. Sin.* **2022**, *42*, 2126004.
58. Guo, X.; Li, B.; Fan, X.; Zhong, J.; Qi, S.; Li, P.; Liu, S.; Wei, B.; Zhao, J. On-demand light wave manipulation enabled by single-layer dielectric metasurfaces. *APL Photonics* **2021**, *6*, 086106. [CrossRef]
59. Ge, S.; Li, X.; Liu, Z.; Zhao, J.; Wang, W.; Li, S.; Zhang, W. Polarization-multiplexed metasurface enabled tri-functional imaging. *Opt. Lett.* **2023**, *48*, 5683–5686. [CrossRef] [PubMed]
60. Du, X.; Shen, W.; Li, J.; Chu, Y.; Sun, J.; Wang, J.; Ji, J.; Chen, C.; Zhu, S.; Li, T. Full-color quasi-achromatic imaging with a dual-functional metasurface. *Nano Lett.* **2025**, *25*, 8143–8150. [CrossRef] [PubMed]
61. Huo, P.; Zhang, C.; Zhu, W.; Liu, M.; Zhang, S.; Zhang, S.; Chen, L.; Lezec, H.J.; Agrawal, A.; Lu, Y. Photonic spin-multiplexing metasurface for switchable spiral phase contrast imaging. *Nano Lett.* **2020**, *20*, 2791–2798. [CrossRef]
62. Zhao, R.; Sain, B.; Wei, Q.; Tang, C.; Li, X.; Weiss, T.; Huang, L.; Wang, Y.; Zentgraf, T. Multichannel vectorial holographic display and encryption. *Light Sci. Appl.* **2018**, *7*, 95. [CrossRef]
63. Hu, Y.; Li, L.; Wang, Y.; Meng, M.; Jin, L.; Luo, X.; Chen, Y.; Li, X.; Xiao, S.; Wang, H. Trichromatic and tripolarization-channel holography with noninterleaved dielectric metasurface. *Nano Lett.* **2019**, *20*, 994–1002. [CrossRef]
64. Liu, M.; Huo, P.; Zhu, W.; Zhang, C.; Zhang, S.; Song, M.; Zhang, S.; Zhou, Q.; Chen, L.; Lezec, H.J. Broadband generation of perfect Poincaré beams via dielectric spin-multiplexed metasurface. *Nat. Commun.* **2021**, *12*, 2230. [CrossRef]
65. Li, X.; Zhou, Y.; Ge, S.; Wang, G.; Li, S.; Liu, Z.; Li, X.; Zhao, W.; Yao, B.; Zhang, W. Experimental demonstration of optical trapping and manipulation with multifunctional metasurface. *Opt. Lett.* **2022**, *47*, 977–980. [CrossRef] [PubMed]

66. Deng, Z.-L.; Deng, J.; Zhuang, X.; Wang, S.; Li, K.; Wang, Y.; Chi, Y.; Ye, X.; Xu, J.; Wang, G.P. Diatomic metasurface for vectorial holography. *Nano Lett.* **2018**, *18*, 2885–2892. [CrossRef] [PubMed]
67. Deng, Z.L.; Jin, M.; Ye, X.; Wang, S.; Shi, T.; Deng, J.; Mao, N.; Cao, Y.; Guan, B.O.; Alù, A. Full-color complex-amplitude vectorial holograms based on multi-freedom metasurfaces. *Adv. Funct. Mater.* **2020**, *30*, 1910610. [CrossRef]
68. Bao, Y.; Ni, J.; Qiu, C.W. A minimalist single-layer metasurface for arbitrary and full control of vector vortex beams. *Adv. Mater.* **2020**, *32*, 1905659. [CrossRef]
69. Bao, Y.; Wen, L.; Chen, Q.; Qiu, C.-W.; Li, B. Toward the capacity limit of 2D planar Jones matrix with a single-layer metasurface. *Sci. Adv.* **2021**, *7*, eabh0365. [CrossRef]
70. Ozawa, T.; Price, H.M.; Amo, A.; Goldman, N.; Hafezi, M.; Lu, L.; Rechtsman, M.C.; Schuster, D.; Simon, J.; Zilberberg, O. Topological photonics. *Rev. Mod. Phys.* **2019**, *91*, 015006. [CrossRef]
71. Lu, L.; Joannopoulos, J.D.; Soljačić, M. Topological photonics. *Nat. Photonics* **2014**, *8*, 821–829. [CrossRef]
72. Li, T.; Liu, M.; Qin, J.; Ren, J.; Hou, J.; Liu, Y.; Yang, X.; Chu, H.; Lai, Y.; Wang, S. Configurable topological photonic polycrystal based on a synthetic hybrid dimension. *Natl. Sci. Rev.* **2025**, *12*, nwaf107. [CrossRef] [PubMed]
73. Yang, X.; Liu, M.; Hou, J.; Li, T.; Wang, S. Topological selective non Hermitian skin effect. *Acta Phys. Sin.* **2025**, *74*, 144205. [CrossRef]
74. Song, Q.; Odeh, M.; Zúñiga-Pérez, J.; Kanté, B.; Genevet, P. Plasmonic topological metasurface by encircling an exceptional point. *Science* **2021**, *373*, 1133–1137. [CrossRef] [PubMed]
75. Yang, Z.; Huang, P.-S.; Lin, Y.-T.; Qin, H.; Zúñiga-Pérez, J.; Shi, Y.; Wang, Z.; Cheng, X.; Tang, M.-C.; Han, S. Creating pairs of exceptional points for arbitrary polarization control: Asymmetric vectorial wavefront modulation. *Nat. Commun.* **2024**, *15*, 232. [CrossRef]
76. Yi, C.; Wang, Z.; Shi, Y.; Wan, S.; Tang, J.; Hu, W.; Li, Z.; Zeng, Y.; Song, Q.; Li, Z. Creating topological exceptional point by on-chip all-dielectric metasurface. *Light Sci. Appl.* **2025**, *14*, 262. [CrossRef]
77. Dorrah, A.H.; Park, J.-S.; Palmieri, A.; Capasso, F. Free-standing bilayer metasurfaces in the visible. *Nat. Commun.* **2025**, *16*, 3126. [CrossRef] [PubMed]
78. Bao, Y.; Nan, F.; Yan, J.; Yang, X.; Qiu, C.-W.; Li, B. Observation of full-parameter Jones matrix in bilayer metasurface. *Nat. Commun.* **2022**, *13*, 7550. [CrossRef]
79. Yang, W.; Zhou, J.; Tsai, D.P.; Xiao, S. Advanced manufacturing of dielectric meta-devices. *Photonics Insights* **2024**, *3*, R04. [CrossRef]
80. Leng, B.; Zhang, Y.; Tsai, D.P.; Xiao, S. Meta-device: Advanced manufacturing. *Light Adv. Manuf.* **2024**, *5*, 117–132. [CrossRef]
81. Jung, C.; Lee, E.; Rho, J. The rise of electrically tunable metasurfaces. *Sci. Adv.* **2024**, *10*, eado8964. [CrossRef]
82. Shaltout, A.M.; Shalaev, V.M.; Brongersma, M.L. Spatiotemporal light control with active metasurfaces. *Science* **2019**, *364*, eaat3100. [CrossRef] [PubMed]
83. Gong, S.; Guo, Y.; Li, X.; Pu, M.; Tian, P.; Zhang, Q.; Chen, L.; Ye, W.; Liu, H.; Zhang, F. Spectral-acoustic-coordinated astigmatic metalens for wide field-of-view and high spatiotemporal resolution 3D imaging. *Light Sci. Appl.* **2026**, *15*, 85. [CrossRef] [PubMed]
84. Zheng, S.; Fu, B.; Zhang, H.; Wang, S. Metalens-Enabled Twisted Chromatic Dispersion. *Adv. Phys. Res.* **2026**, e00003. [CrossRef]

Disclaimer/Publisher's Note: The statements, opinions and data contained in all publications are solely those of the individual author(s) and contributor(s) and not of MDPI and/or the editor(s). MDPI and/or the editor(s) disclaim responsibility for any injury to people or property resulting from any ideas, methods, instructions or products referred to in the content.